ORIGINAL RESEARCH PAPER

Limit states of modern unreinforced clay brick masonry walls subjected to in-plane loading

S. Petry · K. Beyer

Abstract Recent research showed that the in-plane horizontal displacement capacity of unreinforced masonry (URM) walls depends on numerous factors that are not yet captured by current empirical drift capacity models; e.g., axial stress, shear span, geometry of the walls and the material used. In order to improve the performance-based assessment of URM wall buildings, future research should aim at developing numerical and mechanical models that link the global force-displacement response of URM walls to local deformation measures such as strains. This paper addresses the behaviour of modern clay brick masonry and makes first contributions to such an endeavour by the evaluation of experimental results: first, two sets of limit states are proposed that link local damage limit states to characteristic points of the global force-displacement response of the URM wall. The two sets define limit states for walls developing a shear or a flexural mechanism respectively. Second, local deformation measures deemed suitable for the characterisation of these limit states are evaluated from optical measurement data of quasi-static cyclic wall tests. These include strains, compression zone depth and the ratio of shear to flexural deformations.

Keywords Unreinforced masonry · Displacement capacity · Limit states · Performance limits

S. Petry
Earthquake Engineering and Structural Dynamics Laboratory (EESD), School of Architecture, Civil and Environmental Engineering (ENAC), École Polytechnique Fédérale de Lausanne (EPFL), GC B2 515 Station 18, 1015 Lausanne, Switzerland
e-mail: sarah.petry@epfl.ch

K. Beyer (✉)
Earthquake Engineering and Structural Dynamics Laboratory (EESD), School of Architecture, Civil and Environmental Engineering (ENAC), École Polytechnique Fédérale de Lausanne (EPFL), GC B2 504 Station 18, 1015 Lausanne, Switzerland
e-mail: katrin.beyer@epfl.ch

1 Introduction

With the implementation of performance-based principles in design codes (e.g. CEN 2005) not only estimates of the structural elements' stiffness and strength but also of their deformation capacity are required. For URM structural elements, the deformation capacity under horizontal in-plane loading is expressed in terms of storey drift. Today's codes include only rather simple empirical drift capacity models for URM walls (e.g. CEN 2005), which define the drift capacity as a function of only two parameters, i.e., the expected failure mode and the ratio between the shear span and the length of the wall H_0/L. This results in significant dispersion of predicted to observed drift capacities (Frumento et al. 2009; Petry and Beyer 2014a). To promote the use of performance-based design of URM buildings, improved drift capacity models are required. One approach for improving drift capacity models is to consider additional parameters in empirical drift capacity models (e.g. Pfyl-Lang et al. 2011; Petry and Beyer 2014a). However, in the long term, the development of analytical drift capacity models seems desirable. Such models should estimate the drift capacity of a certain limit state (LS) using a mechanical model which links the drift capacity to limits of local deformation measures such as strains and curvatures. For reinforced concrete and steel structures mechanical models for predicting the displacement capacity are well established (e.g. plastic hinge models). For URM walls, first models have been put forward by Priestley et al. (2007) and Benedetti and Steli (2008). These models are limited to cantilever or fixed-fixed walls responding in a rocking mode. The model by Benedetti and Benedetti (2013) includes a shear failure check based on the Mohr-Coulomb criterion; however, their model is still based on a flexural displacement mechanism. In future developments it would be desirable to generalise these models to boundary conditions different to cantilever walls and to develop models that are applicable to walls developing a shear or mixed failure mode.

Thus the objectives for this article are twofold: First, based on findings by other researchers, our own test results on URM walls and the LSs defined in FEMA 306 (ATC 1998), we propose two new sets of LSs which link local damage to characteristic points of the global force-displacement response of URM walls. The two sets define LSs for walls developing a shear or a flexural mechanism respectively. They shall serve as basis for the development of improved mechanical models for the drift capacity of URM walls (Priestley et al. 2007; Benedetti and Steli 2008; Penna et al. 2014). Second, local deformation measures are evaluated that are suited to characterise these LSs. They are computed from optical measurements taken during the test. This information on the local response shall serve also other researchers as input for the validation of models (numerical or mechanical) not only on the global but also on the local level. In the past, often the tests by Ganz and Thürlimann (1984) were used for validation purposes (e.g. Lourenço 1996; Furtmüller and Adam 2011; Facconi et al. 2014). In Zhang et al. (2014), we use the EPFL test data to validate the model developed by Facconi et al. (2014) with regard to global displacements and local strains. Note that all data of this EPFL test series including that of the optical measurements is shared publically via the doi:10.5281/zenodo.8443 allowing hence any researcher to reuse the data (Petry and Beyer 2014b).

After introducing briefly the EPFL tests in Sect. 2, we develop in Sect. 3 the two sets of LSs. In Sect. 4, we evaluate different local deformation measures from the EPFL tests and draw conclusions regarding their suitability to characterise the different LSs. Section 5 summarises the findings and discusses the possibilities and challenges related to the development of mechanical models for the drift capacity of URM walls.

2 Quasi-static cyclic tests on masonry walls

The literature reports the results of a large number of quasi-static tests on URM walls; a summary of these can be found in Frumento et al. (2009). In almost all test series the walls were subjected to either cantilever or fixed-fixed conditions and parameters such as the axial stress ratio and aspect ratio rather than the moment profile over the height of the walls were investigated. Only few test series compare explicitly the behaviour of walls subjected to cantilever and fixed-fixed conditions, e.g. Fehling et al. (2007) and Magenes et al. (2008). These test series demonstrated that the displacement capacity of walls depended on the applied moment profile even if the walls developed the same failure mode.

To complement existing data, a test series of six walls was designed at EPFL to investigate the influence of the two boundary conditions axial stress ratio and moment profile on the force-displacement response of the walls and in particular on their in-plane deformation capacity (Petry and Beyer 2014a, b). In addition to the conventional instrumentation, a LED-based optical measurement system was used to measure the displacement field of the walls, which yielded continuous measurements of local deformation quantities over the entire duration of the tests. In Sect. 2.1, we introduce briefly the test series and compare the walls to other existing series. Section 2.2 discusses the global force-displacement response of the walls and the importance of the discrepancy between chord rotation and interstorey drifts for shear spans different to 1.0 or $0.5H$, where H is the wall height.

2.1 Test programme

The test series comprised six quasi-static cyclic tests of walls with identical dimensions. The parameters that were varied between the tests were the axial stress ratio σ_0/f_u and the ratio between shear span H_0 and wall height H. Both parameters were kept constant in each of the first five tests; for the sixth wall, σ_0/f_u and H_0/H varied in function of the applied lateral force. This test is not included here but more information on the entire test series can be found in Petry and Beyer (2014a, b). In order to simulate an internal wall in buildings with slabs of different stiffness, the first three walls (PUP1–3) were subjected to the same axial stress ratio of $\sigma_0/f_u = 0.18$ but three different shear spans of $H_0 = 0.5, 0.75$ and $1.5H$. The first test, PUP1, was a reference test which applied standard fixed-fixed boundary conditions to the wall. The axial stress ratio σ_0/f_u corresponds to the axial load N divided by the cross section of the wall A and the compression strength of the masonry f_u. Walls 4 and 5 represented external walls. Thus, PUP4 was subjected to an increased axial stress ratio of $\sigma_0/f_u = 0.26$ and an increased shear span of $H_0 = 1.5H$, while PUP5 was tested with $\sigma_0/f_u = 0.09$ and $H_0 = 0.75H$.

The dimensions of all walls were 2.01 m × 2.25 m × 0.20 m (length × height × width). The walls were constructed using a typical modern Swiss hollow-core clay brick and a standard cement mortar (Petry and Beyer 2014b). To record local and global quantities, two kinds of measurement systems were used: a set of conventional instruments recorded forces in all three actuators, the displacement at the top of the wall and average strains of bricks and joints at all four corners of the wall and a LED-based optical measurement system was used to record the displacements of 312 points on the wall. From the optical measurements, the displacement field as well as strains in bricks and deformations in joints could be derived.

In Petry and Beyer (2014a) the resulting displacement capacity of this test series is compared to other 58 existing quasi-static monotonic or cyclic tests on unreinforced clay brick masonry. Comparison showed that the global results from this test series follow the general trends; according to these, the drift capacity decreases with (i) increasing wall size,

(ii) increasing moment restraint at the top of the wall, and (iii) increasing axial stress ratio. In addition, a detailed comparison of global and local quantities, e.g., force-displacement behaviour or crack width, with an equivalent test series at half scale (Petry and Beyer 2014c) showed that the results could be reproduced at reduced scale. From these two studies, we concluded that the behaviour of the EPFL tests is representative of the seismic behaviour of hollow core clay brick masonry with cement mortar.

2.2 Force-displacement envelopes and a comparison of chord rotation and interstorey drift

The test units PUP1–3 were tested applying the same average normal stress ratio but different shear spans. With the pairs PUP2/PUP5 and PUP3/PUP4 the influence of the axial stress ratio was investigated. First cycle envelopes of all five test units are shown in Fig. 1.

While current codes express the displacement capacity of URM walls as interstorey drifts, the deformation of steel or reinforced concrete structural element is often described in terms
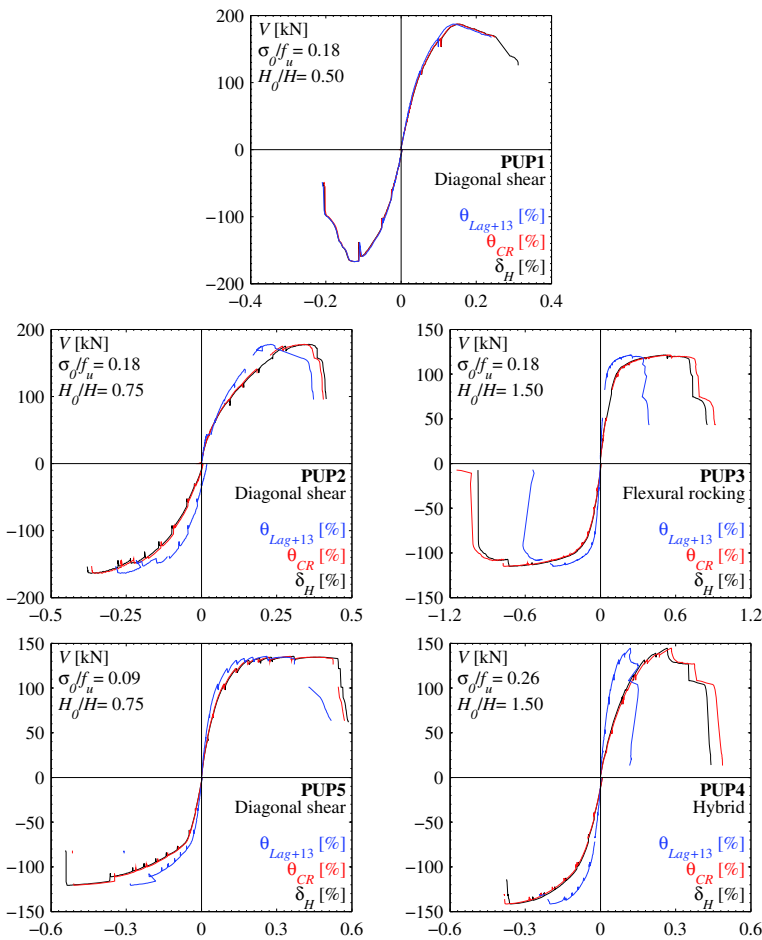
Fig. 1 Force-drift envelopes obtained with the chord rotation θ_{CR}, the interstorey drift δ_H and the drift measure θ_{Lag+13} proposed by Lagomarsino et al. (2013)
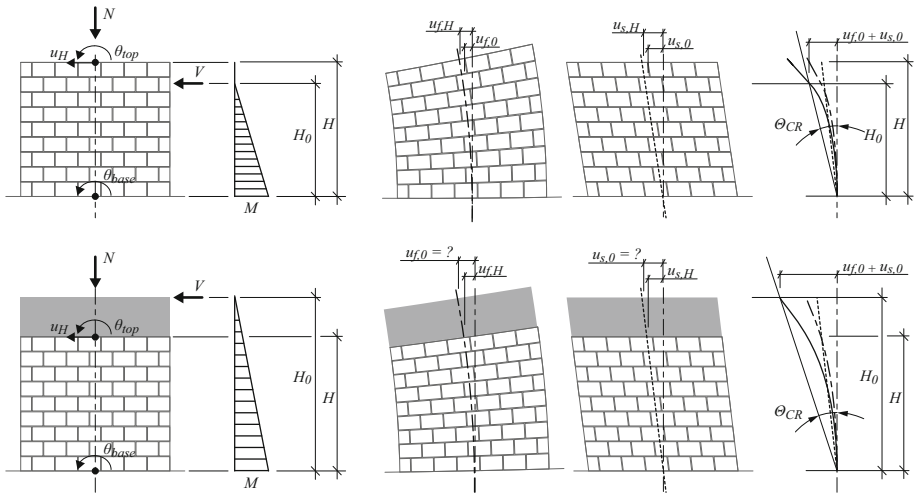
Fig. 2 Definition of the chord rotation for shear spans $H_0 < H$ and $H_0 > H$

of chord rotation, see Fig. 2. When subjected to cantilever or fixed-fixed boundary conditions, interstorey drift and chord rotation are per definition equal (note that, strictly speaking, this assumption does not hold for fixed-fixed boundary conditions if the damage to the top and base of the wall is not identical). Since wall tests reported in the literature applied either of the two boundary conditions, the difference between interstorey drift and chord rotation had not been investigated. The EPFL campaign comprised tests with $H_0/H = 0.75$ and 1.5 and therefore the difference between chord rotation and interstorey drift is of interest. In addition, the drift measure proposed by Lagomarsino et al. (2013) is compared to the interstorey drift and the chord rotation. This drift measure is based on the assumption that the in-plane shear deformation is a better indicator of the wall damage and was originally proposed for the structural member's drift, although in some cases it may coincide with the interstorey drift (Penna, personal communication, Oct. 2014).

The interstorey drift (short: drift) is the total lateral displacement at the top of the wall divided by the storey height (in our case the storey height is equal to the height of the wall H):

$$\delta_H = \frac{u_H}{H} \tag{1}$$

where u_H is the relative horizontal displacement between the top and base of the storey-high wall.

The drift measure proposed by Lagomarsino et al. (2013), which is used to determine the limit states of the bi-linear element in Tremuri, subtracts from the interstorey drift the average rotation at the top and base of the wall:

$$\theta_{Lag+13} = \frac{u_H}{H} - \frac{\theta_{top} + \theta_{base}}{2} \tag{2}$$

where θ_{top} and θ_{base} are the rotation at top and base of the wall respectively. Note that the sign convention is such that (i) θ_{top} is positive if the rotation at the top has the same orientation as the rotation at the top of a cantilever wall subjected to a horizontal load leading to a positive displacement u_H, (ii) θ_{base} is positive in the same sense as the top rotation.

The chord rotation is defined as the lateral displacement at the inflection point divided by the shear span, see Fig. 2.

$$\theta_{CR} = \frac{u_0}{H_0} = \frac{u_{f,0}}{H_0} + \frac{u_{s,0}}{H_0} \tag{3}$$

where $u_{f,0}$ is the flexural component and $u_{s,0}$ is the shear component of the total lateral displacement u_0 at the height H_0. For the walls tested with a shear span $H_0 \leq H$ the displacement at the height of the inflection point can be obtained directly from the LED measurements. For the walls subjected to $\alpha = H_0/H > 1$, however, additional assumptions are required.

Assuming a simple Timoshenko beam with a constant section along its length, we developed the following expression in order to compute the chord rotation from the deformation quantities measured at the top of the wall:

$$\theta_{CR} = \frac{2H_0^2 u_{f,H}}{3H^2 \left(H_0 - \frac{H}{3}\right)} + \frac{u_{s,H}}{H} \tag{4}$$

where $u_{f,H}$ and $u_{s,H}$ are the flexural and shear component of the total lateral displacement at the top of the wall. The first term of the equation is based on a cubic extrapolation of the flexural deformations up to the inflection point, while the second term of the equation is based on a linear extrapolation of the shear deformations. The flexural deformations at the wall height are computed from the difference in rotation at the top and base of the wall; the shear displacement at the top of the wall is computed as difference between total and flexural displacement ($\alpha \geq 1$):

$$u_{f,H} = \left(\theta_{top} - \theta_{base}\right) \cdot \frac{H}{2} \cdot \frac{\alpha - \frac{1}{3}}{\alpha - \frac{1}{2}} \tag{5}$$

$$u_{s,H} = u_H - u_{f,H} \tag{6}$$

For a cantilever wall Eq. (5) yields $2/3 \cdot \theta_{top} \cdot H$, which corresponds to the flexural deformation of a Timoshenko beam. Figure 1 shows the first-cycle envelopes of the five walls, once as function of the drift and once as function of the chord rotation. PUP1 was tested for fixed-fixed condition and accordingly the difference between drift and chord rotation is negligible. PUP2 and PUP5 were both tested with a constant shear span of $0.75H$ and it can be noted that the interstorey drift is slightly larger than the chord rotation. For walls with $H_0 \geq H$ (PUP3 and PUP4) the interstorey drift is slightly smaller than the chord rotation. However, at all stages, the difference between chord rotation and drift is less than 15 % and therefore relatively small. In agreement with the convention in codes, e.g. EC8–P3 (CEN 2005), this paper uses the interstorey drift rather than the chord rotation as measure for the horizontal deformation of the wall.

The drift measure proposed by Lagomarsino et al. (2013) can yield considerable smaller values than the interstorey drift or the chord rotation and therefore the three definitions should not be mixed up. The difference increases with increasing relative rotation between top and base of the wall. This is in particular the case for the walls where $H_0 = 1.5H$. Hence, if the failure of a wall is defined by means of a constant value for θ_{Lag+13} walls with a larger shear span fail at a larger horizontal displacement u_H. Recent research has shown that this failure criterion corresponds better to the observed drift capacities than a constant value of interstorey drift (Petry and Beyer 2014a).

3 Limit states of unreinforced hollow core clay brick masonry walls responding in shear and flexure

The two most common in-plane failure modes of URM walls with hollow core clay bricks subjected to vertical and horizontal in-plane loads are the flexural rocking failure mode and the diagonal shear failure mode. The third failure mode often mentioned in the literature is sliding shear failure along a bed joint. However, for load bearing URM walls with hollow core bricks this failure mode is rarely reported in the literature and was also not observed in the EPFL test series; for this reason it is not included in the following discussion.

As a first step towards describing the kinematics of URM walls, the typical LSs of the walls of the EPFL test series failing in shear and flexure are identified. A LS refers to the first occurrence of a particular crack type or the local failure of parts of the wall. The crack pattern is chosen as parameter for distinguishing the LSs because the appearance of a new type of crack or the concentration of the crack width in a single crack leads typically to a change in the kinematics of the wall. As a result, the modelling hypotheses need to be reconsidered at the LSs. These LSs are then linked to characteristic points of the force-displacement curve of the wall (Sect. 3.1). In a second part, the order of occurrence of these LSs is discussed for the first five walls of the EPFL test series and a link between boundary conditions and the sequence of LSs (Sect. 3.2) is established. The last part of this section shows amplified deformed shapes on which basis the kinematics at the different LSs are discussed (Sect. 3.3).

3.1 Definition of LSs for URM walls

When developing mechanical models for the displacement capacity of URM walls, LSs of the URM walls need to be defined and related to local deformation measures such as strains or crack widths. The LSs should distinguish phases of wall behaviour with different kinematics and describe when local failure mechanisms such as crushing of the bricks occur. As a first step towards such an endeavour, this section defines LSs by means of crack patterns observed for the walls PUP1–5. Two sets of LSs are defined that characterise the behaviour of a shear and flexural prevailing behaviour, respectively. Many walls develop mixed failure modes and feature therefore LSs from both sets.

Note that several researchers defined LSs for URM structures (ATC 1998; Grünthal 1998; Calvi 1999; Abrams 2001; Lang 2002; Bosiljkov et al. 2003; Lagomarsino and Giovinazzi 2006; Tomaževič 2007). Most of these LSs were developed for whole structures. Only FEMA 306 (ATC 1998) and Bosiljkov et al. (2003) address the limit states of individual elements. The newly proposed LSs build on the FEMA 306 LSs in particular for the flexural failure mode. However, the newly proposed LSs differ in two aspects with regard to those in FEMA 306: (i) they focus on crack patterns typical for modern hollow clay brick masonry while FEMA 306 addresses solid clay brick masonry; (ii) each LSs is described by the appearance of a new type of crack which affects the kinematics and does not include the crack width nor the amount of cracking as criteria for the LSs. At the end of this section, the newly proposed LSs are compared to those defined in FEMA 306 (ATC 1998) and Bosiljkov et al. (2003).

F1 to F5 describe five LSs which can be observed when the walls develop a significant flexural behaviour. They are described in Table 1 and illustrated in Fig. 3 with photos of corresponding crack patterns. In Fig. 4 the occurrence of the LSs is indicated in the load-displacement envelopes of the walls. It can be noted that the LS-F1 is associated with a first reduction in wall stiffness. LS-F2, although very apparent in the crack pattern, is not reflected in the force-displacement response of the wall because the masonry below the crack that forms is not an essential part of the load transfer mechanism. LS-F3 refers to the point where

Table 1 Five LSs which can be observed when walls develop a significant flexural behaviour

| LS-F	Local crack pattern	Influence on global response
LS-F1	First appearance of a crack in a bed joint	First reduction of stiffness
LS-F2	Visible separation of the unloaded zone from the compressed zone (Heyman 1992)	Negligible influence on force-displacement response
LS-F3	Appearance of vertical splitting cracks in compressed corner	Peak load is typically attained shortly afterwards
LS-F4	Loss of part of the toe region due to crushing	Significant loss of the lateral resistance
LS-F5	Crushing of entire compression zone	Axial load failure
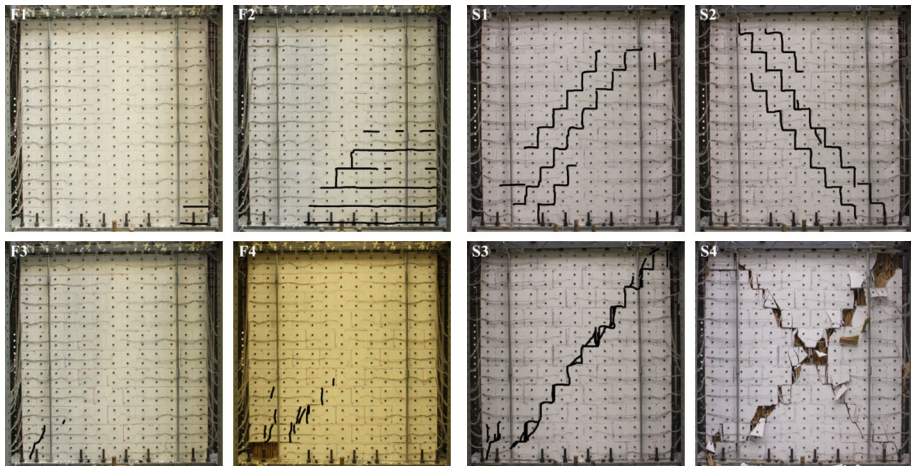
Fig. 3 Photos of different walls of the EPFL test series with the cracks highlighted to show the different LSs caused by flexure (*left*) and shear (*right*): (**F1**) first crack in bed joint, (**F2**) visible separation of the unloaded zone from the compressed zone, (**F3**) cracks in bricks in compressed zone, (**F4**) loss of compressed zone, (**S1**) first stair step crack visible, (**S2**) diagonal shear crack propagates through bricks, (**S3**) concentration of deformation in one diagonal crack and (**S4**) shearing off of the corner bricks

the stress capacity was exceeded in the compressed toe. In the global force-displacement response this LS is typically associated with the maximum shear capacity. After developing the first cracks in the brick at the toe, it was observed that the force capacity did not reduce immediately and only the occurrence of LS-F4 could be associated with a significant loss of lateral resistance. The axial load failure (LS-F5) was attained shortly after.

S1 to S5 describe five LSs which can be observed for shear solicitations. The LSs S1–S5 are described in Table 2 and the corresponding crack patterns are shown in Fig. 3. The first stair step crack (LS-S1) appeared directly over a significant part of the height of the wall and in Fig. 4, it can be noted that LS-S1 was always preceded by a first reduction of stiffness, indicating that the internal load path changed before the stair step crack became visible. The stiffness reduced further with the occurrence of the next LS-S2 and S3. The LS-S3 could be associated with the peak load and the LS-S4 with a significant loss of the
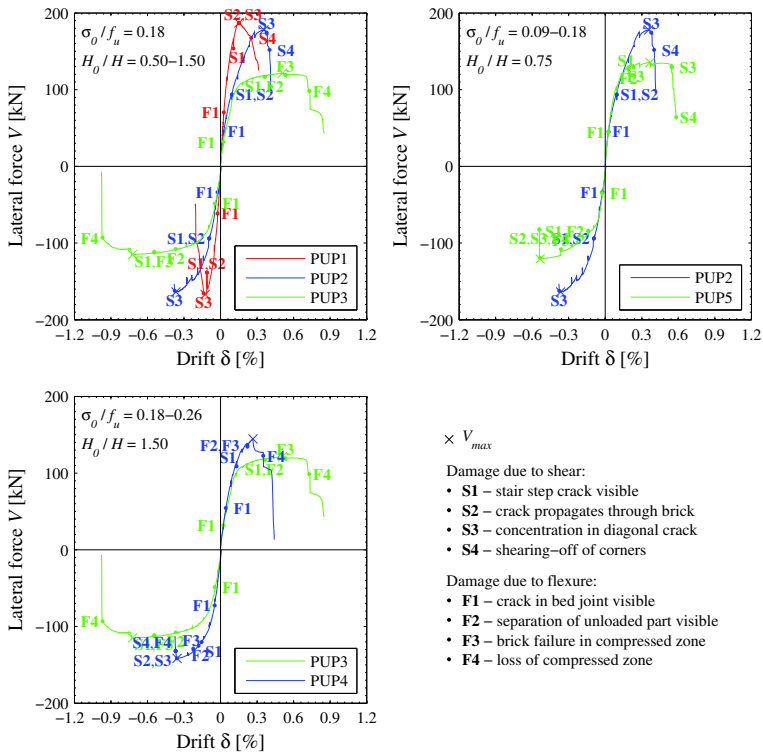
Fig. 4 First cycle envelope of the force-interstorey drift hysteresis for all walls, regrouped according to boundary conditions

lateral resistance. However, once the corner started shearing off (LS-S4), it was observed that strong degradation was introduced to the diagonals under cyclic loading and axial load failure (LS-S5) occurred during the first or second cycles after LS-S4 without a significant increase in the displacement demand.

During testing it was observed that the cracks developing at the LS-S1, F1 and F2 closed again when reversing the loading direction. This observation is also confirmed by the shape of the hysteresis which leads to approximately zero residual drifts at the LS-S1, F1 and F2 (Petry and Beyer 2014b). In fact, these LSs correspond to kinematic states where cracks did not propagate through the bricks yet (see also Tables 3 and 4). On the other hand, the LSs which comprise cracks in bricks (S2–S4 and F3–F4) must depend on the type of brick used for the construction of the URM walls, e.g., brittleness of the brick, and the possibility of the cracks to propagate, e.g., loading velocity and loading history.

To set the newly proposed LSs into context, we compare in Tables 3 and 4 the proposed LSs to the LSs of URM walls defined in FEMA 306 (ATC 1998) and Bosiljkov et al. (2003). The FEMA 306 defines the LSs "insignificant damage" to "extreme damage" for different kinds of structural elements, including URM walls, in function of crack pattern and crack width. The LSs defined by Bosiljkov et al. (2003) are based on the performance rather than the crack pattern, e.g., the limit state "life safety". The comparison in Tables 3 and 4 is thus to a certain degree subjective as the three different scales use different identifiers. In addition, FEMA 306 (ATC 1998) provides λ-factors which describe the ratio of the remaining to the

Table 2 Five LSs which can be observed when walls develop a significant shear behaviour

LS-S	Local crack pattern	Influence on global response
LS-S1	First appearance of diagonal stair step cracks in mortar joints (Mann and Müller 1982)	Preceded by a first reduction of stiffness
LS-S2	First appearance of vertical and inclined cracks through bricks along the diagonals	Negligible influence on force-displacement response
LS-S3	Deformations start concentrating in one diagonal crack	Peak load is typically attained shortly afterwards
LS-S4	Shearing off of the corners of the bricks	Significant loss of the lateral resistance
LS-S5	Crushing of bricks along the diagonal crack	Axial load failure

Table 3 Comparison of the newly proposed set of LSs for flexure with existing LSs for URM walls and their recommended reduction factors for stiffness (λ_K), strength (λ_Q) and displacement capacity (λ_D)

Newly proposed LSs				Bosiljkov et al. (2003)	FEMA 306 (ATC 1998)			
LS-F	Reduction (PUP3)			Performance levels	Damage levels	Reduction		
	λ_K	λ_Q	λ_D			λ_K	λ_Q	λ_D
LS-F1	1.0	1.0	1.0	First crack	Insignificant	1.0	1.0	1.0
LS-F2	1.0	1.0	1.0	–	Moderate	0.8	1.0	1.0
LS-F3	0.8	1.0	1.0	Life safety	Heavy	0.6	0.9	1.0
LS-F4	0.35	0.65	1.0	Collapse prevention	Extreme	0.4	0.8	0.7
LS-F5	–	–	–	–	–	–	–	–

initial properties once a certain LS was attained. Such λ-factors are defined for the stiffness (λ_K), the strength (λ_Q) and the displacement capacity (λ_D) and allow therefore defining the bi-linear force-displacement response of an element that reached a certain LS. To compare the different definitions of LSs, we determine these factors on the basis of the test results for PUP1 and PUP3 and compare these to the values in FEMA 306 in Tables 3 and 4. It can be seen that the values in FEMA 306 tend to be conservative when compared to our values. Only for LS-S4, FEMA 306 overestimates the remaining capacity, which might be due to the fact that the hollow clay brick masonry is more brittle than the solid clay masonry walls, on which FEMA 306 is based.

3.2 Influence of boundary conditions on the drift for which the LSs are attained

In Fig. 4, the different LSs are indicated in the first cycle envelopes of the five EPFL walls. Figure 4a compares the walls subjected to the same axial stress ratios but different shear spans: as expected, the stiffness decreases with increasing shear span. The larger the shear span, the smaller the drift for which flexural cracks developed in bed joints (F1) and for which the unloaded part separated from the loaded part of the wall (F2). As a result, the larger the shear span, the smaller the drift for which a first decrease in stiffness was observed. A smaller shear span caused, however, significant diagonal stair step shear cracks (S1 of

Table 4 Comparison of the newly proposed set of LSs for shear with existing LSs for URM walls and their recommended reduction factors for stiffness (λ_K), strength (λ_Q) and displacement capacity (λ_D)

Newly proposed LSs				Bosiljkov et al. (2003)	FEMA 306 (ATC 1998)			
LS-S	Reduction (PUP1)			Performance levels	Damage levels	Reduction		
	λ_K	λ_Q	λ_D			λ_K	λ_Q	λ_D
LS-S1	1.0	1.0	1.0	Immediate occupancy	Insignificant	1.0	1.0	1.0
LS-S2	0.95	1.0	1.0	–	Insignificant	1.0	1.0	1.0
LS-S3	0.8	0.9	0.9	Life safety	Moderate	0.8	0.9	1.0
LS-S4	0.5	0.55	0.25	Collapse prevention	Heavy/extreme	0.4	0.8	0.7
LS-S5	–	–	–	–	–	–	–	–

Table 5 Drift in (%, rounded to 0.05 %) for which the LSs (F1/F2/F3/F4) associated to flexural solicitation occurred ("NO" = not observed)

σ_0/f_u; H_0/H	0.5	0.75	1.5
0.09	–	0.025/0.15/0.25/0.55	–
0.18	0.025/NO/NO/NO	0.025/NO/NO/NO	0.025/0.35/0.55/0.9
0.26	–	–	0.05/0.15/0.2/0.35

Table 6 Drift in (%, rounded to 0.05 %) for which the LSs (S1/S2/S3/S4) associated to shear solicitation occurred ("NO" = not observed)

σ_0/f_u; H_0/H	0.5	0.75	1.5
0.09	–	0.15/0.35/0.55 / 0.6	–
0.18	0.1/0.15/0.15/0.25	0.1/0.1/0.35/0.4	0.45/NO/NO/NO
0.26	–	–	0.15/0.35/0.35/0.35

PUP1 and PUP2). These spread also quickly through the bricks (S2) and provoked thus a significantly more abrupt horizontal and axial load failure than for walls with a larger shear span (PUP3), which failed in a flexural mode due to crushing of the toe (F4). However, in Fig. 4, it can be noted that the LSs associated with the loss of the corner bricks (LS-S4/F4) are both immediately succeeded in the envelope by axial load failure. Therefore, S5 and F5 are omitted in the following.

Figure 4b, c show walls subjected to the same shear span but different axial stress ratios: Walls tested with the same shear span had similar initial stiffnesses. The lower axial stress ratio favoured the development of flexural deformations in PUP3 and PUP5 (e.g. F1 and F2) and caused thus an earlier softening of these walls. On the other hand the increased axial stress ratio favoured the development of non-reversible LSs (e.g. S2 and F3) and provoked thus a more abrupt failure for these walls (PUP2/PUP4 versus PUP5/PUP3). The drift values for which the different damage states were observed are summarized in Tables 5 and 6. When a LS was observed for both loading directions, the average drift is given. These tables show that the drifts for which the different LSs are attained decrease with increasing axial stress ratio.
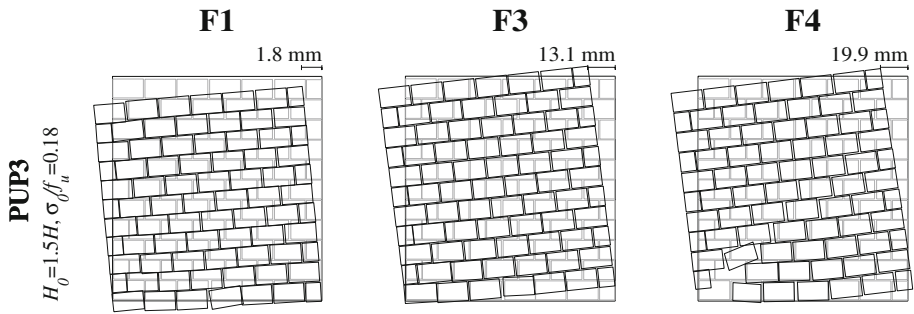
Fig. 5 Amplified deformation shapes for a wall (PUP3) developing a significant flexural mode at LS-F1, F3 and F4

3.3 Kinematics of URM walls at different LSs

The kinematics of URM walls depend first of all on the prevailing behaviour mode (flexure vs. shear) but vary also throughout the loading history. The LSs defined in the previous section identify points when the kinematics of the walls changes due to the appearance of a new type of crack. In order to visualise the different kinematics of the walls, we show the amplified deformed shapes of the wall that developed the most significant flexural mode (PUP3) and shear mode (PUP1), respectively. The displacements are shown with respect to the zero measurement before the axial load was applied (LS0, Petry and Beyer 2014b).

3.3.1 Amplified deformed shapes at flexural LSs

Figure 5 shows the amplified deformed shapes of the wall which developed the most significant flexural mode (PUP3, note that due to the high amplification factor for smaller displacements the brick seem to overlap). The deformed shapes are plotted for LS-F1 (crack in bed joint visible), F3 (splitting cracks in compressed zone) and F4 (partial loss of compressed zone). The figure shows that for LS-F1 the lateral deformations develop mainly through a shortening of the wall on the compression side. Once bed joints start to open up (F1), the compressed length of the wall reduces until first splitting cracks appear (F3) and the onset of toe crushing (F4). When LS-F3 and F4 are reached, the compressed length has reduced so much that large deformation concentrate in the bottom brick layers of the wall and the wall seems to rotate as a rigid body around its base.

3.3.2 Amplified deformed shapes at shear LSs

Figure 6 shows the amplified displaced shapes of the wall which developed the most significant shear mode (PUP1, note that due to the high amplification factor for smaller displacements the brick seem to overlap). The displaced shapes are plotted at LS-S1 (stair step crack visible), S3 (concentration of deformation in one diagonal crack) and S4 (shearing-off of bricks in corner). At LS-S1, a clear diagonal compression strut develops, along which first inclined stair step cracks open up. With increasing displacement demands, deformations start to concentrate along one crack which follows the geometric diagonal of the walls. Thus, at LS-S3, the wall separates into two triangles, which are held together by the corner bricks and form two almost independent parts. This separation of the wall into two triangles is a con-
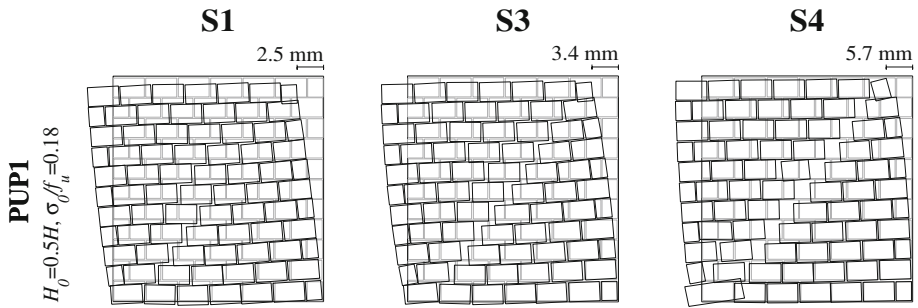
Fig. 6 Amplified deformation shapes for a wall (PUP1) developing a significant shear mode at LS-S1, S3 and S4

tinuous process which initiates at LS-S1 and causes the softening in the force-displacement curve, which we observed in Sect. 3.2 from LS-S1 onwards.

However, once the deformation start concentrating in one diagonal crack, sliding occurs at the centre of the diagonal crack (see the relative displacement between both triangles in Fig. 6 at LS-S3). At this state, the global displacement capacity of the walls is given by the flexural and shear deformation of the separated triangles (see the bended triangles in Fig. 6 at LS-S3) and further by the ability of the triangles to transfer the shear stresses through their tips. Thus, the corner bricks are highly solicited and once the brick strength is exceeded there, the corner bricks collapse (LS-S4). This causes a significant sliding movement that occurs along the whole length of the diagonal crack (see Fig. 6) and involves always a significant loss of lateral strength. Note that similar damage are described in the literature for numerical models of URM walls, e.g., for the solid clay URM wall modelled by Lourenço and Rots (1997) with a multi-surface interface model.

4 Local deformation measures for characterising different LSs

In a mechanical model, global and local deformation quantities have to be linked through a kinematic model. Since failure occurs locally, LSs should be identified through limits of local deformation (e.g. strains and crack width) or local strength (e.g. compression and shear strength). To investigate which local deformation measures could be suitable for such an endeavour, different deformation quantities are computed from the optical measurement results and their properties at different LSs are discussed. The considered deformation measures are vertical and shear strain fields (Sect. 4.1) as well as strain profiles at the outer edges of the wall (Sect. 4.2), bed joint openings (Sect. 4.3), curvatures (Sect. 4.4) and shear strains (Sect. 4.5).

4.1 Vertical strain and shear strain fields at different LSs

In Sect. 3.3, it is mentioned that large parts of the deformations originate from the shortening of the compression struts (see Figs. 5, 6) which results thus in a bending of the wall. This can be best visualised by strain fields. In order to homogenize the anisotropy of the masonry, strains are computed as average strains of one brick and one mortar layer. To do so, virtual LEDs are defined at midheight of the bricks. Their displacement is computed from the average displacement of the LEDs above and below, which are glued onto the same brick
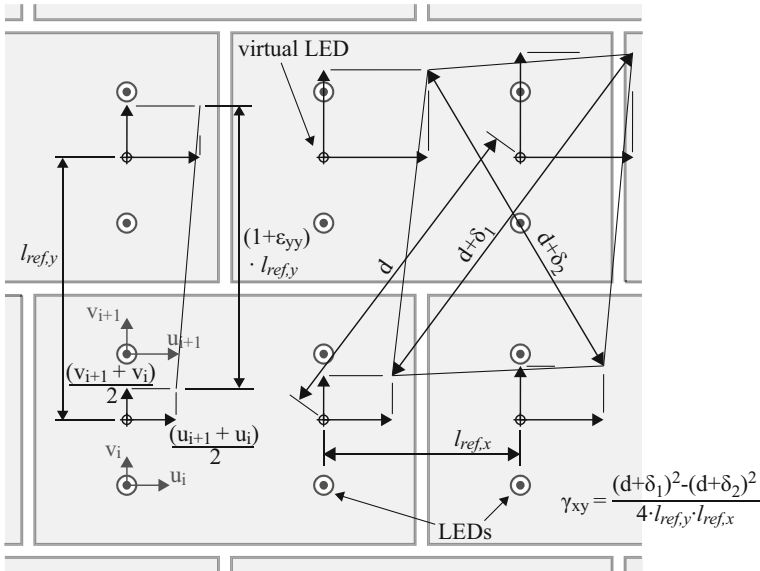
Fig. 7 Schema showing how vertical strains ε_{yy} and the shear strains γ_{xy} are computed
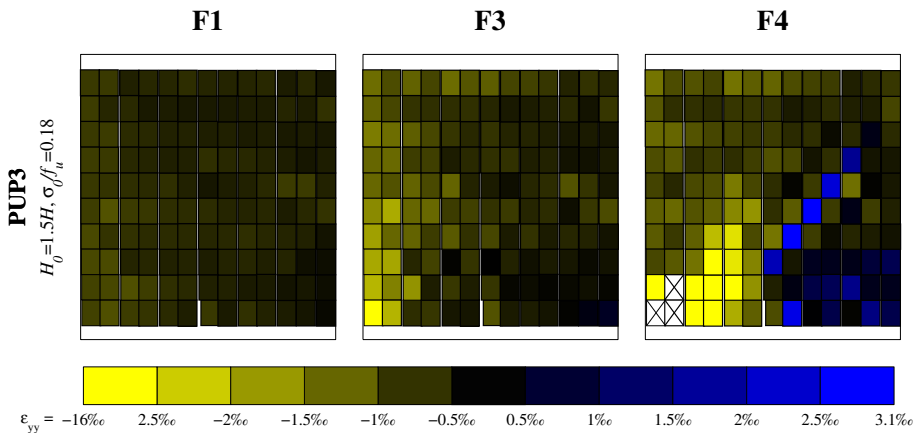

Fig. 8 Vertical strain ε_{yy} measured between two layers of brick for a wall (PUP3) developing a significant flexural mode at LS-F1, F3 and F4

(see Fig. 7). Vertical strains ε_{yy} and shear strains γ_{xy} of the masonry are computed on the basis of the displacements of these virtual LEDs (see Fig. 7). All deformations are computed with reference to the measurement taken before the vertical load was applied (LS0, Petry and Beyer 2014b).

4.1.1 Strain fields at flexural LSs

Figures 8 and 9 show the vertical and shear strain fields of PUP3, which developed a significant flexural mode at LS-F1, F3 and F4. The considered wall (PUP3) was tested with a shear span larger than the wall height and accordingly, the compression strains concentrate along one
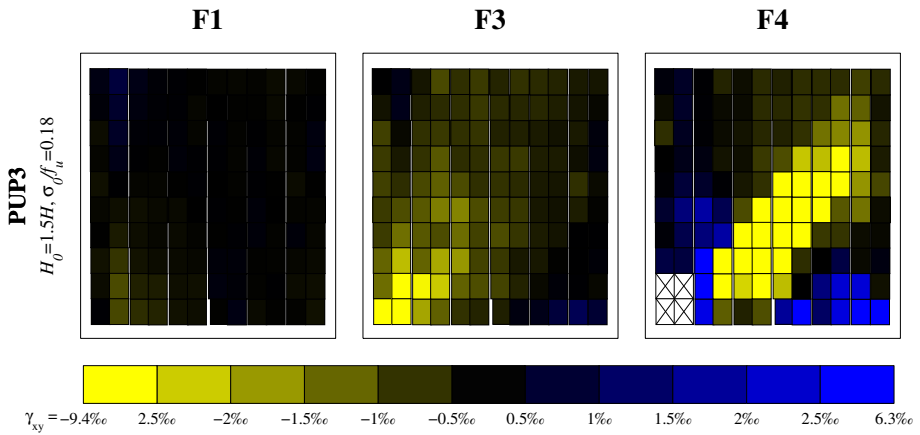
Fig. 9 Shear strains γ_{xy} at the LS-F1, F3 and F4 for a wall (PUP3) developing a significant flexural mode
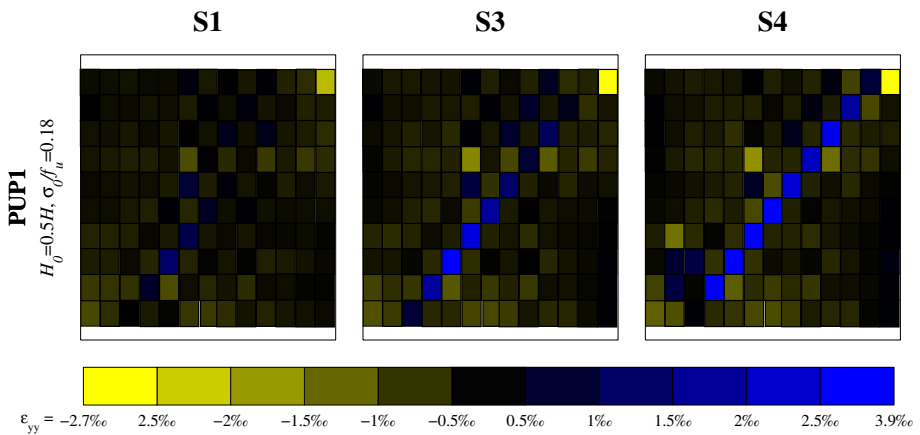
Fig. 10 Vertical strain ε_{yy} at the LS-S1, S3 and S4 for a wall (PUP1) developing a significant shear mode

side (left wall edge in Fig. 8), while tension strains developed on the other side (right wall edge in Fig. 8). Once the compressed length is significantly reduced, deformations start concentrating at the wall base, which is reflected in the large axial strains and shear strains in the bottom left corner for LS-F3/F4 in Figs. 8 and 9.

4.1.2 Strain fields at shear LSs

Figures 10 and 11 show the vertical and shear strains for a wall (PUP1) developing a significant shear mechanism at LS-S1, S3 and S4. In Fig. 10, the diagonal crack opening is clearly visible in form of a stair step dark blue line. Assuming that the vertical head joints are stress free, the shear stresses τ_{xy} are transferred from brick layer to brick layer solely by the bed joints. This subjects the brick to a torque moment, which is countered by a pair of differential vertical stresses $\Delta\sigma_{yy}$ that are superimposed to the mean vertical stresses σ_{yy} (Mann and Müller 1982). When this pair of differential stresses $\Delta\sigma_{yy}$ exceeds the mean vertical stresses σ_{yy}, the brick starts to uplift on one side resulting in an opening of the bed joint over half the brick
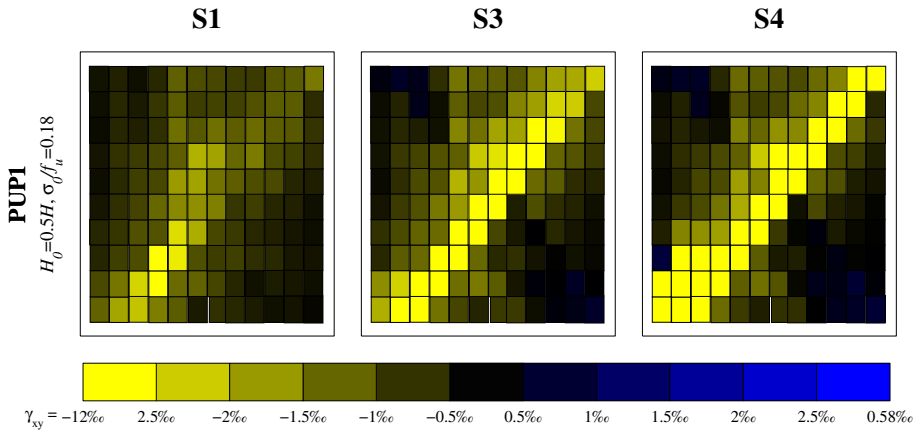
Fig. 11 Shear strain γ_{xy} at the LS-S1, S3 and S4 for a wall (PUP1) developing a significant shear mode
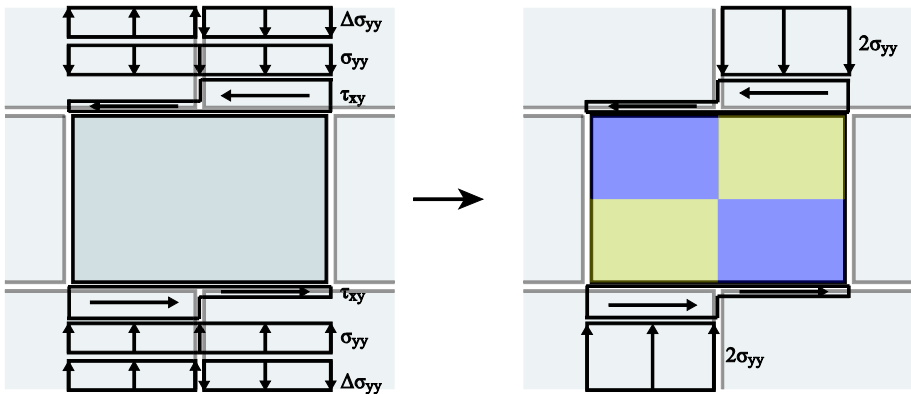
**Fig. 12** Partial uplift of bricks due to local torque of brick; adapted from Mann and Müller (1982)

length (Fig. 12). This is reflected in Fig. 10 by the alternating blue and yellow rectangles along the diagonal of the wall.

In Sect. 3, it was noted that first several parallel diagonal cracks developed (LS-S1/S2) but eventually the crack opening tends to concentrate in a single diagonal crack (LS-S3). After that, two triangles form which are held together at the corners until local stresses exceed the capacity of the corner bricks (LS-S4), see Fig. 13. Figure 10 confirms these observations: once separation of the two triangles occurs (LS-S3), the vertical strains next to the diagonal crack increase. This indicates that one load path passes through the upper and one load path through the lower triangle. In both triangles the major compression struts run parallel to the diagonal crack. These struts force the triangles to bend and to develop flexural cracks in the bed joints as shown in Fig. 13.
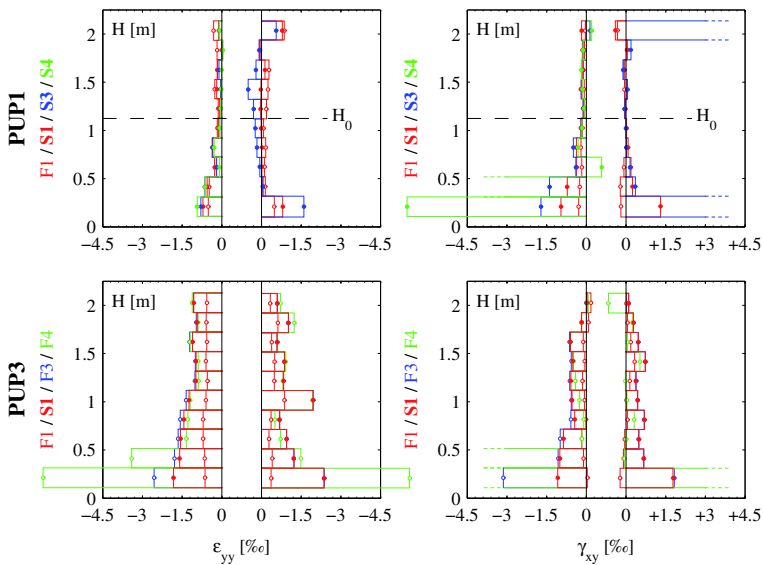
4.2 Vertical and shear strain profiles at the outer edges of the walls at the different LSs

The strain fields in the previous section visualised the force flow through the masonry walls. The axial and shear strain fields highlighted the high demands on the compressed toes of
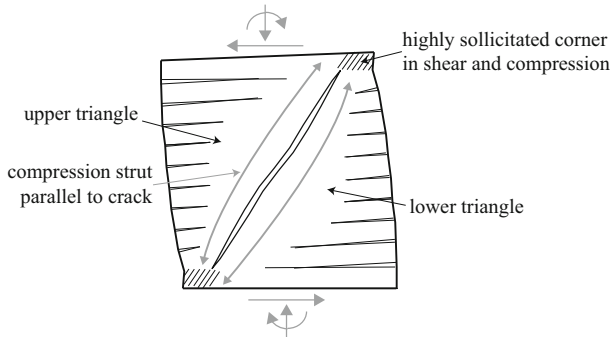
Fig. 13 Crack pattern and force flow after occurrence of LS-S3

Fig. 14 Strain profiles of the compressed edges for the different LSs for a wall developing a significant flexural (PUP3) mode and a wall developing a significant shear mode (PUP1)

the walls, i.e., compression failure of the toe (LS-F3/F4) or shearing off of the corner bricks (LS-S4), and the flow of forces along the diagonal crack (LS-S3). As a first step towards quantifying admissible deformation limits for the compressed toes, the strain profiles of the compressed edge are shown. The vertical strains ε_{yy} and the shear strains γ_{xy} are computed as described in Fig. 7 using the outmost lines of LEDs (the distance between the first outmost line of LEDs and the edge of the walls is approximately 8 cm). In order to differentiate between the two loading directions, the origin of the x-axes is slightly offset (see Fig. 14).

In Fig. 14, a significant increase of vertical strains towards the lower layers of the wall can be noted. Even though the compression strains are higher for the walls developing a significant flexural mode (PUP3), the concentration of vertical strains in the bottom layers of the masonry is visible for both walls. In addition, also the shear strains concentrate in the lower brick layers of the masonry wall and confirm thus the high solicitation of the corner

bricks. Independent of the prevailing mechanism, the shear strains in the corner bricks are of the same amplitude for both walls before reaching LS-S3/F3.

4.3 Bed joint opening for the different walls at the different LSs caused by flexure

The opening of the first horizontal joint occurred for nearly all walls for rather small drift demands ($\sim$0.025 %, Fig. 4) leading to a first reduction of stiffness. The effective stiffness of the wall depends on the compressed length. If mechanical models shall be able to describe fully the flexural mode, good estimates for the actual compressed length are required. In the following, we investigate whether plane section analysis and neglecting the tensile strength of the URM (e.g. Benedetti and Steli 2008) leads to good estimates of the compressed length. For flexural failure, the maximum moment is limited by the overturning moment and once the compressed length is reduced significantly, the moment starts approaching the overturning moment $M = NL/2$ asymptotically (e.g. Penna et al. 2014). The theoretical point of decompression of the bed joints is computed from the axial load N, the length of the wall L and the moment M using plane section analysis ($M = NL/6$). For the wall tests considered here, N is constant throughout the test, while the moment M depends on the applied horizontal force, the shear span H_0 and the distance of the bed joint to the base of the wall. Assuming a linear-elastic behaviour for the masonry in compression and zero tensile strength, the compressed length can be estimated as (e.g. Benedetti and Steli 2008):

$$L_c = 3\left(\frac{L}{2} - \frac{M}{N}\right) \quad \text{for } M > NL/6 \tag{7}$$

For computing the compressed length from the optical measurements the following approach was used (see Fig. 15): first the rigid body displacements (u_b, v_b) and rotation (θ_b) and the deformations ($\varepsilon_{b,xx}$, $\varepsilon_{b,yy}$ and $\gamma_{b,xy}$) of each brick are evaluated from the displacement of the four LEDs on one brick. All deformations are computed with reference to the measurement LS0 performed before axial load application (Petry and Beyer 2014b). Assuming that the strain state is uniform in the entire brick, the vertical and horizontal displacements at the top and bottom edge of each brick are computed ($u_{j,top}$, $v_{j,top}$ and $u_{j,bottom}$, $v_{j,bottom}$, see Fig. 15) and the deformation of a joint is obtained by comparing the displacement of two adjacent bricks. Finally, the compressed length is defined as the distance between the external wall edge in compression and the position at which the joint first opens ($v_{j,top} - v_{j,bottom} > 0$).

In Fig. 16, the measured compressed length for a wall showing a significant flexural (PUP3) and a wall showing a significant shear failure mode (PUP1) are plotted versus the theoretical compressed length L_c for the base joint and the second joint using Eq. (7). The moment is normalized by dividing it by the limit overturning moment $NL/2$. It can be observed that the moment demand in the shear dominated wall (PUP1) is too small to develop a significant opening at the base, while for the flexural dominated wall (PUP3) the compressed length of the bottom and second joint decreases to $\sim$0.2 and $\sim$0.25 L, respectively. Hence, we concluded that Eq. (7) leads to good estimates of the compressed length as long as no significant diagonal crack has formed.

4.4 Curvature at the different LSs caused by flexure

In previous sections we show that an important part of the total displacement capacity of all walls originates from flexural deformations. This applies also to the walls that eventually failed in shear (e.g. PUP1, Fig. 6). In general, flexural deformations can be best described by
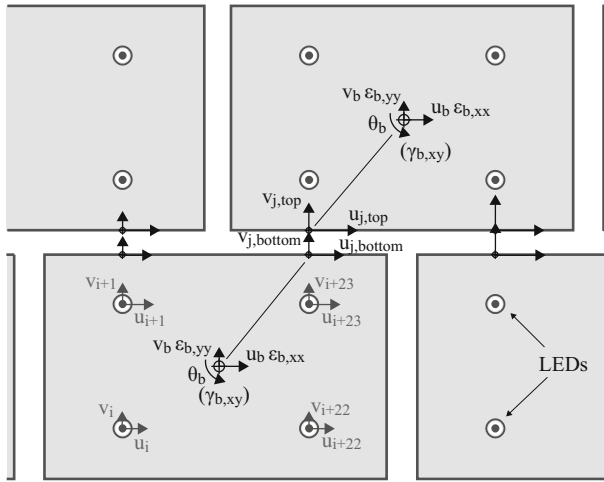
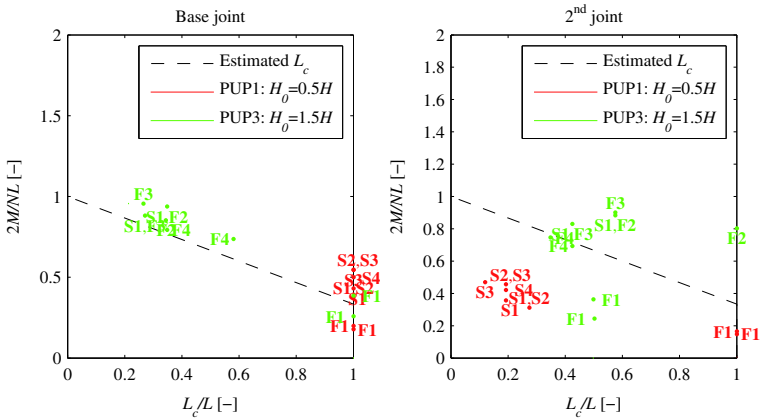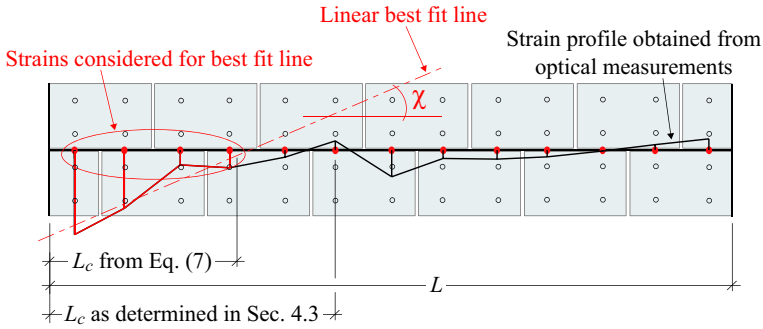**Fig. 15** Schema showing how the opening of the bed joints is evaluated

Fig. 16 Moment vs captured compressed length portion in base and 2nd joint at the observed LSs for a wall developing a significant flexural mode (PUP3) and a wall developing a significant shear mode (PUP1)

curvatures and therefore the evaluation of curvatures suggests itself. Hence, in the following we compute the curvatures using the vertical strains ε_{yy} from Sect. 4.1. Since the part in compression controls the wall's behaviour, first the theoretical compressed length L_c is estimated using Eq. (7) and then the curvature is determined as slope of the best fit line of the vertical strains obtained from the LEDs for which the distance to the edge in compression is shorter than L_c (see Fig. 17).

In Fig. 18, the resulting curvature profiles are plotted for the different LSs for the walls PUP1 and PUP3. The curvature profiles correspond to average values from curvatures in the positive and negative loading direction at the same LS. Hence, the curvature profiles are only included when the LSs are obtained for both loading directions. For PUP1 it can be noted that once the deformation start concentrating along one diagonal crack at LS-S3 and the hypothesis of plane sections clearly no longer holds, the curvature profile turns very irregular. This conclusion is in agreement with the conclusion from Sect. 4.3 on the prediction

Fig. 17 Schema showing how the curvature is obtained from the vertical strain profile
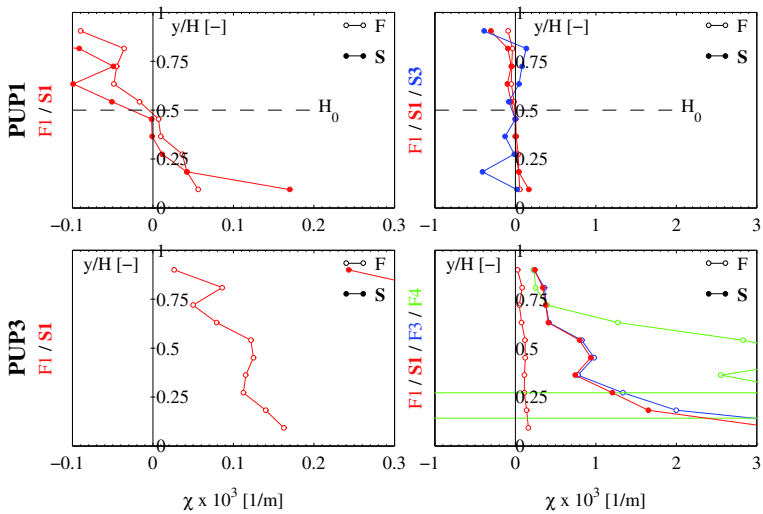

Fig. 18 Curvature profiles at the LS-F1 to S4 when considering only the part of the masonry in compression

of the bed joint opening using Eq. (7). By contrast, the shapes of the curvature profiles before S3 are rather regular and it seems feasible to estimate these by a simple analytical model. For example, the height of zero curvature of these profiles intersects with the y-axes at approximately the height of zero moment. Furthermore, for LSs up to F1 (opening of bed joints) the curvature profile is approximately linear. Once the bed joints start opening, the compressed area reduces and the deformations start concentrating in the lower brick layers of the masonry (see Figs. 8, 10, 14 in Sects. 4.1, 4.2). In Fig. 18, it can be seen that for the LSs succeeding LS-F1 this concentration of deformations is reflected in an over proportional increase of curvatures at the base.

4.5 Shear strains at the different LSs caused by shear solicitation

The curvature profiles are an indicator for the flexural deformability. However, taking into account that URM walls can be rather squat, shear deformations can contribute in equal measure to the total deformations as flexural deformations. Thus, in this section the shear strain profiles are investigated. Assuming again that the compressed part of the wall controls
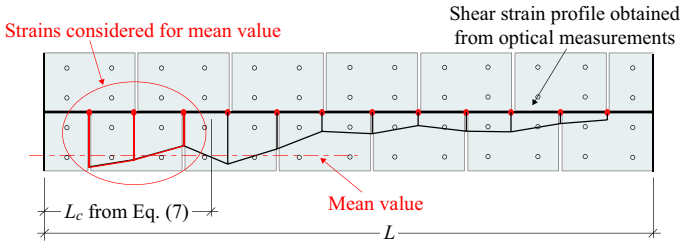
Fig. 19 Schema showing how the shear strain is obtained from the shear strain profile
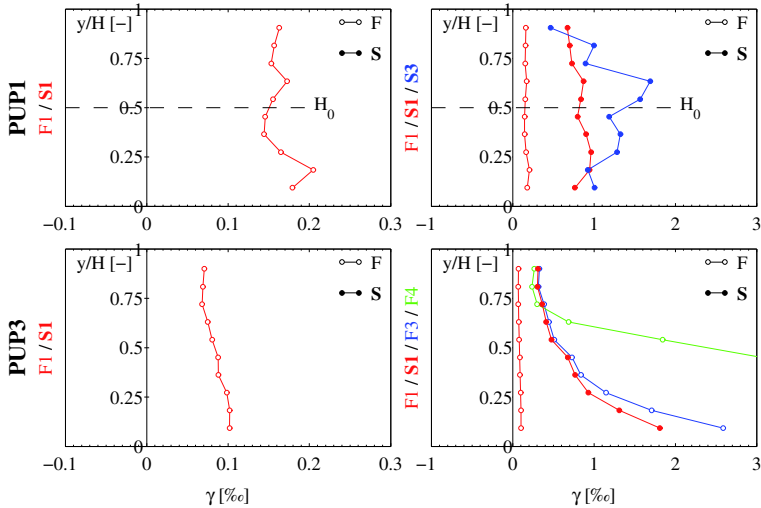
Fig. 20 Shear strain profiles at LS-F1 to S4 when considering only the part of the masonry in compression

the wall's behaviour, the shear strain at a particular height is computed as average of the shear of the compressed section at this height (see Fig. 19). The shear strains themselves are computed using the approach described in Fig. 7.

In Fig. 20, the shear strain profiles correspond to average values of the shear strains in the positive and negative loading direction at the same LS. The shear strain profiles are only included when the LSs are attained for both loading directions. It can be noted that the shear strains are rather constant over the height for small displacement demands (LS-S1/F1), while for higher displacement demands the shears strains tend to increase towards the base. This is due to the fact that after the first opening of the base joint at LS-F1, the effective section reduces and shear and compression stresses concentrate in the compressed zone. Since stresses and strains are related, this phenomenon is well visible for PUP3 (see also Fig. 14). Similar to the curvature profiles (see previous section), the shear strain profiles turn quite irregular once the walls start separating into two triangles (LS-S3).

5 Conclusions

Drift capacity models in current codes are based on empirical relationships but in the long term a replacement with analytical drift capacity models seems desirable (Petry and Beyer

2014a). Such models should estimate the drift capacity at a certain limit state (LS) using a mechanical model which links the global force-displacement response of URM walls to local deformation measures such as strains and curvatures. However, in order to develop such models, local deformation measures that characterize the different LSs need to be identified.

Based on the observations by others (Mann and Müller 1982; Heyman 1992), results of our own tests and the LSs defined in FEMA 306 (ATC 1998), we define two sets of local LSs which are based on the occurrence of new cracks and therefore involve changes in the kinematics of the walls. For flexural modes, LS-F1 to F5 describe five LSs from the first appearance of a horizontal crack in the bed joint (F1) up to the instant when the wall loses its axial load bearing capacity (F5). For shear modes LS-S1 to S5 describe the behaviour of the wall from the appearance of first stair step crack (S1) up to the instant when the upper triangle slips abruptly downwards (S5), which leads to both horizontal and axial load failure. We discuss the cause of these different LSs and we show that the drifts for which the different LSs are attained decrease with increasing axial stress and with decreasing shear span. We then link these LSs to characteristic points of the global force-displacement response.

In a second part of the paper we evaluate different local deformation measures at these LSs for two walls developing a shear and flexural failure mode respectively. The vertical and shear strain fields underline the high solicitation of the corner regions and along the diagonal crack. Furthermore, the strain fields show that the deformation behaviour of the considered URM walls is controlled by the compressed part of the wall. Accordingly, in the following, the deformations of the compressed part of the wall are investigated in detail and the curvature and shear strain profiles of the compressed wall part are evaluated from the experimental measurements. The results suggest that before the formation of a diagonal shear crack, the wall behaviour can be described by a Timoshenko beam where the variable cross section over the height of the wall corresponds to the compressed part of the wall. After the formation of the diagonal crack, the kinematics of the wall change and the wall behaves like two triangles above and below the diagonal crack. From this point onwards, a new kinematic model needs to be applied, which is yet to be developed.

References

Abrams DP (2001) Performance-based engineering concepts for unreinforced masonry building structures. Prog Struct Mat Eng 3(1):48–56

ATC (1998) FEMA-306: evaluation of earthquake damaged concrete and masonry wall buildings. Basic Procedures Manual, Applied Technology Council (ATC), Washington

Benedetti A, Benedetti L (2013) Interaction of shear and flexural collapse modes in the assessment of in-plane capacity of masonry walls. In: Proceedings of the 12th Canadian masonry symposium, Vancouver, Canada

Benedetti A, Steli E (2008) Analytical models for shear-displacement curves of unreinforced and FRP reinforced masonry panels. Constr Build Mater 22:175–185

Bosiljkov V, Page A, Žarnič R (2003) Performance based studies of in-plane unreinforced masonry walls. Mason Int 16(2):39–50

Calvi GM (1999) A displacement-based approach for vulnerability evaluation of classes of buildings. J Earthq Eng 3(3):411–438

CEN (2005) Eurocode 8: design of structures for earthquake resistance: part 3: assessment and retrofitting of buildings EN 1998-3:2005. European Committee for Standardisation, Brussels, Belgium

Facconi L, Plizzari G, Vecchio F (2014) Disturbed stress field model for unreinforced masonry. J Struct Eng 140(4). doi:10.1061/(ASCE)ST.1943-541X.0000906

Fehling E, Stuerz J, Emami A (2007) D 7.1a Test results on the behaviour of masonry under static (monotonic and cyclic) in plane lateral loads. Technical report of the collective research project ESECMaSE

Frumento S, Magenes G, Morandi P, Calvi GM (2009) Interpretation of experimental shear tests on clay brick masonry walls and evaluation of q-factors for seismic design. Technical report, IUSS PRESS, Pavia, Italy

Furtmüller T, Adam C (2011) Numerical modeling of the in-plane behavior of historical brick masonry walls. Acta Mech 221:65–77. doi:10.1007/s00707-011-0493-z

Ganz HR, Thürlimann B (1984) Versuche an Mauerwerksscheiben unter Normalkraft und Querkraft. Test report 7502-4, ETH Zürich, Switzerland (in German)

Grünthal G (ed.), Musson R, Schwarz J, Stucchi M (1998) European Macroseismic Scale 1998, Cahiers de Centre Européen de Géodynamique et de Seismologie, vol 15, Luxembourg

Heyman J (1992) Leaning towers. Meccanica 27:153–159

Lagomarsino S, Giovinazzi S (2006) Macroseismic and mechanical models for the vulnerability and damage assessment of current buildings. Bull Earthq Eng 4:415–443

Lagomarsino S, Penna A, Galasco A, Cattari S (2013) TREMURI program: an equivalent frame model for the nonlinear seismic analysis of masonry buildings. J Eng Struct 56:1787–1799. doi:10.1016/j.engstruct.2013.08.002

Lang K (2002) Seismic vulnerability of existing buildings. PhD Thesis, ETH Zürich, Switzerland

Lourenço PB (1996) Computation strategies for masonry structures. PhD Thesis, TU Delft, Netherlands

Lourenço PB, Rots JG (1997) Multisurface interface model for analysis of masonry structures. J Eng Mech 123(7):660–668

Magenes G, Morandi P, Penna A (2008) D 7.1c Test results on the behaviour of masonry under static cyclic in plane lateral loads. Technical report of the collective research project ESECMaSE

Mann W, Müller H (1982) Failure of shear-stressed masonry: an enlarged theory, tests and application to shear walls. In: Proceedings British Ceramic Society, vol 30, pp 223–235

Penna A, Lagomarsino S, Galasco A (2014) A nonlinear macroelement model for the seismic analysis of masonry buildings. Earthq Eng Struct Dyn 43(2):159–179. doi:10.1002/eqe.2335

Petry S, Beyer K (2014) Influence of boundary conditions and size effect on the drift capacity of URM walls. Eng Struct 65:76–88. doi:10.1016/j.engstruct.2014.01.048

Petry S, Beyer K (2014b) Cyclic test data of six unreinforced masonry walls with different boundary conditions. Earthq spectra. doi:10.1193/101513EQS269

Petry S, Beyer K (2014c) Scaling unreinforced masonry for reduced-scale seismic testing. Bull Earthq Eng. doi:10.1007/s10518-014-9605-1

Priestley MJN, Calvi GM, Kowalsky MJ (2007) Displacement-based seismic design of structures. IUSS Press, Pavia

Pfyl-Lang K, Braune F, Lestuzzi P (2011) SIA D 0237: Evaluation de la sécurité parasismique des bâtiments en maçonnerie. Documentation SIA D 0237 (in French). Swiss society of engineers and architects (SIA), Zürich, Switzerland

Tomaževič M (2007) Damage as a measure for earthquake-resistant design of masonry structures: Slovenian experience. Can J Civ Eng 34(11):1403–1412

Zhang S, Petry S, Beyer K (2014) Investigating the in-plane mechanical behavior of URM piers via DSFM. In: Second European conference on earthquake engineering and seismology, Istanbul, Turkey